Y. Grebenyuk, H.X. Zhang, M. Wilhelm, K. Rezwan, M.E. Dreyer

Wicking into porous polymer-derived ceramic monoliths fabricated by freeze-casting

Recommended Citation (primary publication/Version of Record) incl. DOI:

Y. Grebenyuk, H.X. Zhang, M. Wilhelm, K. Rezwan, M.E. Dreyer,
Wicking into porous polymer-derived ceramic monoliths fabricated by freeze-casting,
Journal of the European Ceramic Society, Volume 37, Issue 5, 2017, Pages 1993-2000, ISSN 0955-2219,
https://doi.org/10.1016/j.jeurceramsoc.2016.11.049

Wicking into porous polymer-derived ceramic monoliths fabricated by freeze-casting

Y. Grebenyuk[a], H.X. Zhang[b], M. Wilhelm[b,*], K. Rezwan[b,c], M.E. Dreyer[a]

[a] Department of Fluid Mechanics, Center of Applied Space Technology and Microgravity (ZARM), Faculty of Production Engineering, University of Bremen, Am Fallturm, 28359 Bremen, Germany
[b] Advanced Ceramics, University of Bremen, Am Biologischen Garten 2, 28359 Bremen, Germany
[c] MAPEX – Centre for Materials and Processes, University of Bremen, Am Fallturm 1, 28359 Bremen, Germany

ARTICLE INFO

Article history:
Received 14 September 2016
Received in revised form
25 November 2016
Accepted 29 November 2016
Available online 20 December 2016

Keywords:
Anisotropic porous structure
Freeze-casting
Capillary transport
Wicking
Lucas–Washburn equation

ABSTRACT

Silicon oxycarbide monoliths of different pore size distribution were fabricated by freeze-casting. The samples revealed a lamellar pore structure with an axial anisotropy. To evaluate the capillary transport abilities we performed wicking experiments. The sample weight measurement method was applied during the imbibition. The samples show deviations in permeability from 10% to 49% at different sample orientations that quantifies the impact of the anisotropy in the axial direction. The deviations were larger for the samples with smaller pore size. For these samples we also observed larger differences in the wicking behaviour. The samples with bigger pore size demonstrated higher permeability and faster wicking. Imbibition results at both sample orientations showed a good agreement with a prediction via the Lucas–Washburn equation with gravity effects. We demonstrate hereby, that our approach of macroscopic modelling predicts wicking behaviour in anisotropic structures reasonably well, providing a simple tool for further porous material investigations.

1. Introduction

Transport processes in porous materials have found a wide range of applications. Heat and mass transfer processes are of particular interest for heat pipes technologies [1,2] and catalyst support in chemical reactors [3–5]. Mass transport and structure characteristics are essential for filtration technologies [6–8]. Moreover, porous materials are applied in space industry for phase separation and transport of storable and cryogenic fluids. For example, propellant management devices (PMD), or liquid acquisition devices (LAD), enable a gas-free propellant delivery to the engines due to capillary pressure driven flows in porous elements and the corresponding bubble point pressure [9–11]. A gas port phase separator has been proposed to prevent liquid expulsion via the gas ports of propellant tanks using double porous screen elements [12,13]. Moreover, special attention has recently been drawn to anisotropic porous materials [14–16]. The properties of these materials are directionally dependent. That allows to adjust porous structures to particular needs of certain devices and to improve their performance.

The application of porous ceramics for transport processes may increase technical efficiency and reduce production and maintenance costs. Properties of porous ceramics including high specific surface area, chemical and thermal stability, corrosion resistance and controllable surface characteristics can be adjusted by applying different techniques, like sacrificial templating, direct foaming or freeze casting method, which give different structures and pore size ranges [8,17,18]. For the spaceflight community a substantial benefit is the relatively light weight of porous ceramics compared to metallic elements used nowadays. However, porous ceramics have to fulfil the requirements of the aerospace industry concerning mechanical integrity and cleanliness.

Imbibition, or wicking, is a spontaneous penetration of liquid into porous media due to capillary forces. This process can be used to investigate capillary transport abilities of porous materials. Some studies have already been done to examine this ability in porous ceramics. Einset [19] analyzed the capillary rise of organic liquids into a porous medium fabricated of consolidated particles of C and SiC via the tape casting method. The author optically measured the penetration heights as a function of time and determined the corresponding infiltration rates. Kumar et al. [20] investigated organic liquid infiltration in porous carbon–carbon preforms. The authors applied optical measurements to determine penetration heights and estimated the flow rate of water through porous media

* Corresponding author.
E-mail addresses: yulia.grebenyuk@zarm.uni-bremen.de (Y. Grebenyuk), mwilhelm@uni-bremen.de (M. Wilhelm).

http://dx.doi.org/10.1016/j.jeurceramsoc.2016.11.049
0955-2219/

to characterize permeability. In a second paper, Kumar et al. [21] studied the infiltration rates of silicone in porous carbon–carbon preforms. Okada et al. [22] estimated capillary rise properties of porous mullite ceramics prepared by an extrusion method. The capillary rise height in experiments with water was determined by visual observation. Okada et al. [23] also examined the imbibition into porous geopolymers prepared by an extrusion method.

Nevertheless, to the author's extent of knowledge no experiments have been performed to investigate the capillary transport abilities of anisotropic porous ceramics. We studied wicking into silicon oxycarbide (SiOC) cylindrical samples fabricated by a freeze-casting method. The lamellar pore structures with an axial anisotropy and different pore size distribution were prepared. The sample weight measurement technique was applied to obtain the mass increase of the imbibed liquid. That allowed to obtain the experiment data disregarding the assumption of a flat wicking front necessary for the optical determination of the wicking rate. In order to investigate the influence of the axial anisotropy on the imbibition, experiments were performed at various sample orientations. In addition, wicking results were compared to some theoretical model prediction.

2. Experimental procedure

2.1. Preparation of porous ceramics

The porous monolith was prepared according to the previously published method by Zhang et al. [24] with minor modification. The H44 (methyl phenyl polysiloxane) derived filler loading was 30% in weight, and a freeze dryer was used instead of a climate chamber to remove the ice, which reduced the thermal stresses at the surface, resulting in a smooth monolith surface. The process scheme is shown in Fig. 1. Silica sol here worked as a binder as well as a water source. The reason of using silica sol as a water source is to improve the mechanical properties of the green body as well as the pyrolyzed monolith [24]. Cylindrical aluminum molds with a

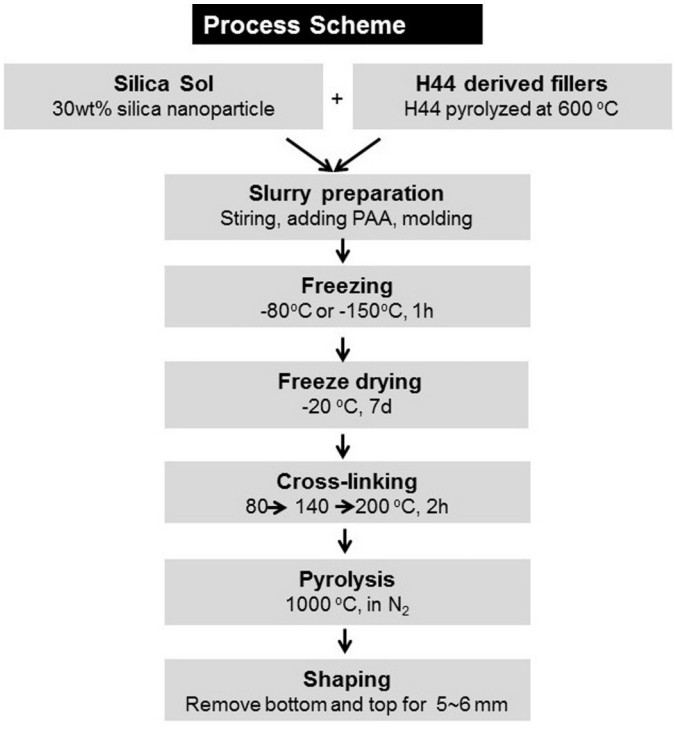

Fig. 1. Preparation of the monolith by freeze casting method and shaping. Figure modified from [24].

height of 60 mm, an inner diameter of 35 mm and a wall thickness of 2 mm were put on the bottom of the freezer at −80 °C or at −150 °C for 1 h. The freezing temperature was varied to obtain structures of different pore size distributions. After the pyrolysis, 5–6 mm of the bottom and the top part of the monoliths were cut off to get a symmetric porous structure required for macroscopic modelling of the imbibition.

In this work, SiOC was chosen due to the low thermal conductivity and heat capacity of this material. The investigation of the capillary transport behaviour of porous ceramics was aimed at solving cryogenic propellant transport. Therefore, the thermal conductivity and the heat capacity of the studied porous monolith should be relatively low for this application. SiOC material cannot be prepared with ceramic powders directly, and normally it is prepared with preceramic polymers by pyrolysis, during which the preceramic polymer will convert to SiOC materials. Due to the large size of the monolith and the small and uniform pore size needed for the capillary transport, the water based freeze casting technique was used to fabricate the macroporous SiOC monolith. To prepare such a bulky monolith, two pyrolysis processes have been used. The first pyrolysis was used to convert the hydrophobic H44 into hydrophilic H44 derived filler, which can only be used in the water based freeze casting process. The second pyrolysis step was used to consolidate the green body, while more bonds were formed, which can increase the mechanical strength. The details can be found in [24].

In the following, the samples prepared at the freezing temperature of −80 °C are referred as to 80-1 and 80-2, while the samples prepared at −150 °C as to 150-1 and 150-2. The geometrical characteristics of the samples are summarized in Table 1.

2.2. Characterization

The particle size and pore morphology of the samples was analyzed via scanning electron microscopy (SEM, Camscan Series 2, Obducat CamScan Ltd.). The samples were sputtered with gold (K550, Emitech, Judges Scientific plc.) before the measurements. Mercury intrusion porosimetry (Pascal 140/440, POROTEC GmbH) was used to determine the macroporosities. For the pore size calculation, a cylindrical model was chosen, and the pore size was calculated by the Washburn equation. The average diameter was calculated based on the derivative principle. The porosity range within which the porosimeter works was subdivided into 50 intervals, which determined the calculation sensitivity. The pore range to perform the measurement of the average radius was set from 0 to 200 μm. The derivative of the volume of mercury penetrated (namely the pores volume) versus the variation of the diameter for each of the selected intervals was performed by the instrument software. The interval with maximum penetration of mercury was selected, namely where the largest volume of pores was located, and here the average radius was calculated within the selected range, see Table 1.

2.3. Wicking experiment

Fig. 2 shows a schematic image of the setup for the wicking experiments. The weight of a porous sample was measured using an electronic high precision balance (LA 310S-0CE, Sartorius) with an accuracy of ±0.0001 g. The balance was fixed on a height-adjustable platform driven by two stepper motors (VRDM566/50, Berger Lahr/Schneider Electric) with a velocity of 0.38 mm/s. The sample was placed in a closed vessel of 0.095 m diameter partly filled with FC-72 liquid supplied by 3M Fluorinet™. Some thermophysical properties of FC-72 liquid are listed in Table 2. Due to perfect wetting characteristics of the FC-72 test liquid the contact angle with regard to the experimental samples was taken as

Table 1
Geometrical characteristics and macroscopic parameters of the porous samples. D and L are referred as to the overall diameter and length of the cylindrical monolith, respectively. d is referred as to the diameter of the cone area with upward oriented pores that is visible from the bottom of the monolith. R_{av} and ϕ_{merc} are referred as to the average pore radius and the open porosity determined via the mercury intrusion porosimetry. The values of the open porosity ϕ_{imb} and permeability K_{-z} and K_{+z} determined from imbibition experiments at $-z$ and $+z$ sample orientations are shown with a standard deviation for four test runs.

Sample	D (m) 10^{-3}	d (m) 10^{-3}	d/D (–)	L (m) 10^{-3}	R_{av} (m) 10^{-6}	ϕ_{merc} (–)	ϕ_{imb} (–)	K_{-z} (m^2) 10^{-14}	K_{+z} (m^2) 10^{-14}	K_{-z}/K_{+z} (–)
80-1	30	21	0.70	42	8.35	0.532	0.466 ± 0.002	4.43 ± 0.10	3.65 ± 0.12	1.21
80-2	30	19	0.63	42	8.35	0.532	0.471 ± 0.003	5.00 ± 0.22	4.48 ± 0.12	1.12
150-1	30	21	0.70	42	1.57	0.548	0.516 ± 0.007	0.265 ± 0.003	0.177 ± 0.002	1.49
150-2	30	15	0.50	42	1.57	0.548	0.516 ± 0.005	0.368 ± 0.007	0.336 ± 0.002	1.10

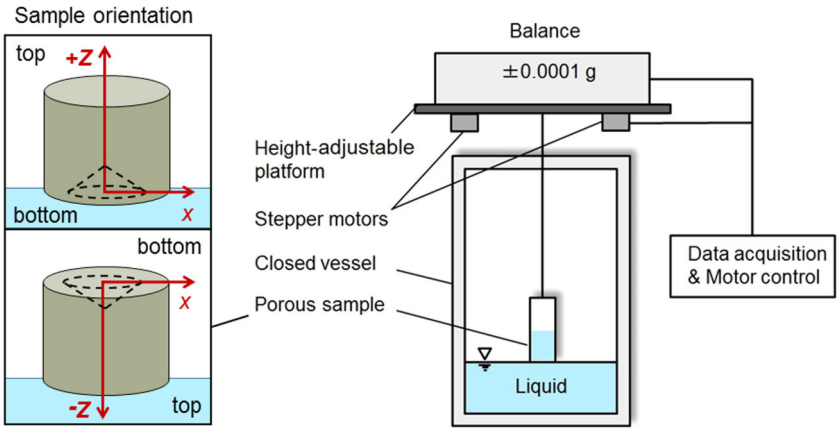

Fig. 2. The schematic image of the setup for wicking experiments. Each sample was tested using "bottom to top" and "top to bottom" orientation to the liquid surface. These orientations are referred as to $+z$ and $-z$, respectively.
Figure modified from [25].

Table 2
Density ρ_L, dynamic viscosity μ_L and surface tension σ of FC-72 liquid at 101,325 Pa and 298.15 K.

ρ_L (kg m^{-3})	μ_L (Pa s) 10^{-6}	σ (Nm^{-1}) 10^{-3}
1690	709.8	12

zero. The tests were performed at room temperature and normal pressure. In order to initiate the wicking, a vertically oriented porous sample was submerged into the bulk liquid by a depth of approximately 3 mm. The liquid imbibed into the unsaturated (not submerged) part of the sample. The imbibition caused a sample weight increase that was recorded with a sampling rate of 20 Hz. A constant sample weight at the end of the imbibition indicated complete saturation of the sample. To finish the experiment the sample was driven approximately 6 mm upwards and, thus, detached from the liquid surface.

To study the impact of the anisotropy on the wicking process each sample was tested using "bottom to top" and "top to bottom" orientation to the liquid surface, see Fig. 2. In the following, we refer to these orientations as to $+z$ and $-z$, respectively. Four test runs were performed for each sample and each sample orientation.

Some corrections of the weight measurements were required to account for buoyancy, the Wilhelmy effect and the liquid level decrease due to the imbibition of the liquid into the samples. The sample weight changes caused by the liquid level decrease due to wicking could be eliminated using geometrical characteristics of the samples and of the experimental vessel. However, the buoyancy force could not be calculated accurately due to the uncertainty in the determination of the submersion depth (± 1 mm). The Wilhelmy force estimates a contribution of the outer meniscus, formed at the sample perimeter, upon contact of the sample with the liquid surface [26,27]. Nevertheless, for porous media the accurate determination of this force was not possible.

Moreover, the sample weight changes due to buoyancy and the Wilhelmy effect are difficult to separate from the early wicking process. Therefore, the correction of the sample weight measurements we performed following an approach proposed by Grebenyuk and Dreyer [25]. The total contribution of buoyancy and the Wilhelmy effect could be estimated if the liquid level decrease was corrected or negligible. The final weight of a completely saturated but still partly submerged sample has been subtracted from the actual weight of the saturated sample. The total correction of the sample weight measurements for experimental samples was found to be up to 12%.

3. Results and discussion

3.1. Macroporous structure

A shrinkage of around 14% in radial direction was found for all the green bodies after pyrolysis at 1000 °C. However, there are no cracks observed. The macroporous structure of the monolith was determined by the temperature gradient during the freezing process. The freeze rate was controlled by applying different freezing temperatures. Water forms lamellar ice, which results in lamellar pores inside the ceramics after ice sublimation, resulting in an anisotropic porous structure of the material. Due to the cylindrical aluminum mold, the lamellar ice will grow from metal surface to the inner part. At the bottom part of the monolith, the ice grew upwards, forming a cone structure, which also happened at the top. However, the thermal conductivity of the solid in the freezing slurry was much lower than aluminum, therefore, the temperature gradient from the radial direction dominated in the monolith. In the middle part of the monolith, only radial lamellar pores were formed. The top and bottom were partially removed to

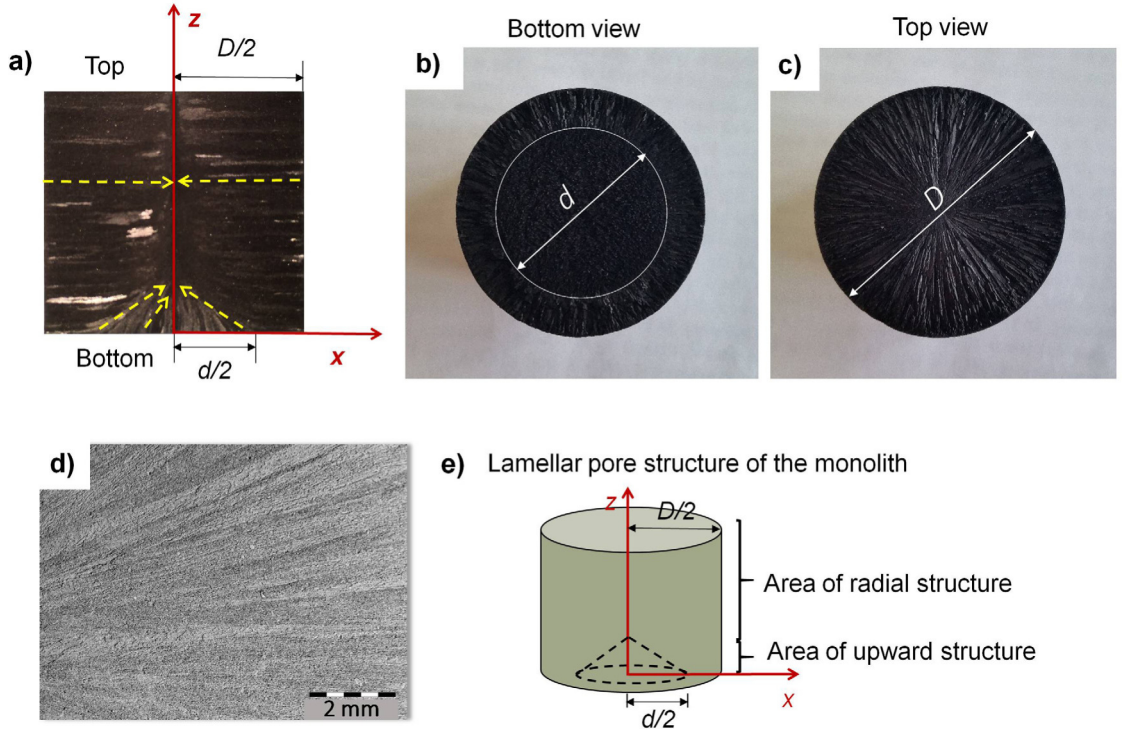

Fig. 3. (a) The side view of the longitudinal cross-section of the monolith. The yellow dash lines indicated the directions of the lamellar pores; (b) the bottom view of the monolith; (c) the top view of the monolith; (d) the SEM of the transverse cross-section at the top; and (e) the scheme of the anisotropic structure. *D* is referred as to the overall diameter of the cylindrical monolith and *d* is referred as to the diameter of the cone area with upward oriented pores that is visible from the bottom of the monolith.

get a cylindrical symmetric monolith. The symmetry is an essential assumption for macroscopic modelling of wicking. The upward lamellar structure at the bottom was preserved and the diameter of this area is *d*, which can be altered by cutting, see Table 1. As seen from Fig. 3(a), the parallel lines indicate the lamellar pores parallel to the radial direction, which can be partly seen in Fig. 3(d).

From the SEM, the lamellar pores, defined as the distances between the lamellae, were along radial direction (*x* axis in Fig. 3(a)) and show distances of around 20–50 μm and less than 10 μm for the samples frozen at −80 °C and −150 °C, respectively. The bridges between two adjacent lamellae were created by dendrites growth of ice. Depending on the freeze rate, the lamellar aspect ratios can be manipulated, as can be seen from Fig. 4(a) and (b). The mercury intrusion porosimetry in Fig. 4(c) and (d) showed that the monolith frozen at −80 °C had a porosity of 53.2% and pore size range of mainly 10–100 μm with relatively wide pore size distribution. The monolith frozen at −150 °C has an open porosity of 54.8%, a pore size of mainly 3–8 μm with a narrow pore size distribution. Samples prepared at two different freezing temperatures have similar cylindrical symmetric structures, which were formed by the similar temperature gradient direction, controlled by the mold. However, lower freeze temperature resulted in smaller pore sizes, which could influence the wicking performance.

3.2. Macroscopic parameters

The characterization of the capillary transport abilities of porous media required the knowledge of macroscopic parameters, such as the open porosity, the characteristic pore radius, and the permeability.

We determined the open porosity of the structures using the mercury intrusion porosimetry ϕ_{merc}, see Section 3.1 and Table 1. Nevertheless, hardware limitations of the setup for the mercury intrusion porosimetry allowed to test only some sample cuts to obtain ϕ_{merc}. Therefore, this macroscopic parameter was also computed using the results of the weight measurements of dry samples and samples completely saturated with FC-72 liquid. Thus, the open porosity ϕ_{imb} could be calculated using

$$\phi_{\mathrm{imb}} = \frac{V_{\mathrm{void}}}{V_{\mathrm{total}}} = \frac{m_{\mathrm{L}}/\rho_{\mathrm{L}}}{V_{\mathrm{total}}}, \tag{1}$$

where V_{total} is the total volume of a sample, V_{void} is the void volume of a sample that includes only the volume of interconnected pores, and ρ_{L} is the density of the liquid. The results for each sample are summarized in Table 1. The values of ϕ_{merc} and ϕ_{imb} obtained using two different methods are in good agreement. However, for further calculations we used ϕ_{imb}, which is a volume-averaged value of the open porosity determined for the whole structure. This is of importance for the macroscopic modelling of the wicking process.

In order to estimate the characteristic pore size of the structures we used the results of the mercury intrusion porosimetry, see Section 3.1. The average pore size was calculated in a pore size interval with the largest volume of pores. The pore diameters of 16.7 μm and 3.14 μm were obtained for the structures prepared at the freezing temperature of −80 °C and −150 °C, respectively. The corresponding values of the average pore radii are summarized in Table 1.

The characterization of the ability of a porous structure to conduct a flow through it is of importance for capillary transport processes. A macroscopic parameter that quantifies such a property of a porous media is the permeability *K* that is commonly defined via Darcy's law [28,29]. Due to the anisotropy of our samples with respect to vertical wicking, this parameter was examined for both sample orientation, +*z* and −*z*. In order to determine the permeability, we performed wicking experiments and applied the method proposed by Fries et al. [30]. The flow through porous media was implied analogous to the flow through a bundle of capillary tubes and the macroscopic approach was employed for the description of the imbibition. For smaller times the capillary

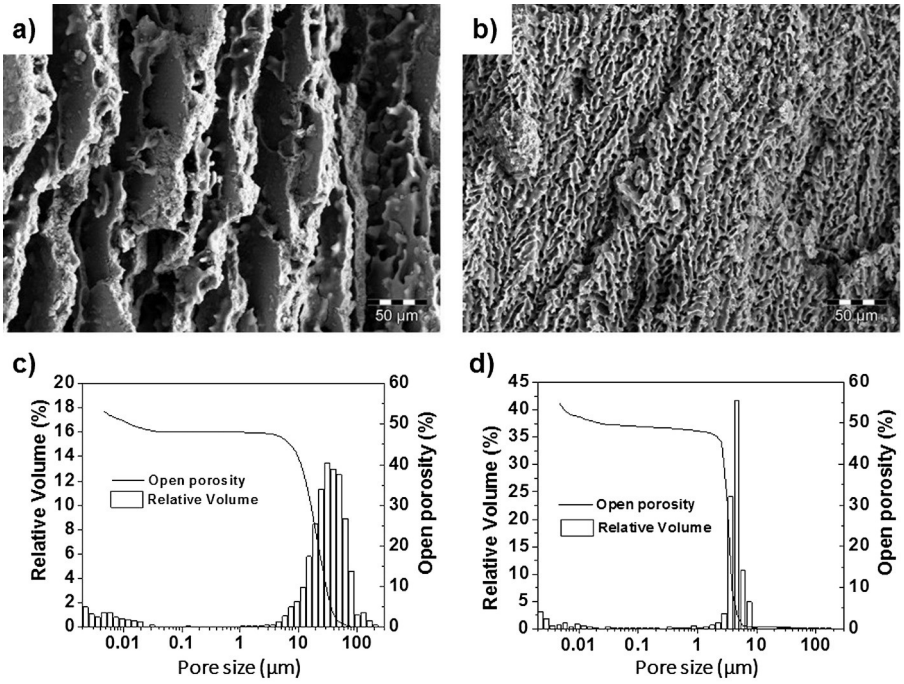

Fig. 4. SEM images of pyrolyzed monoliths with the cross-section perpendicular to the monolith axis (a and b) frozen at −80 °C and −150 °C, respectively. (c and d) Pore size distribution versus relative pore volume and open porosity curves obtained from the mercury intrusion porosimetry of pyrolyzed samples.

rise is dominated by inertia and viscous forces [35]. However, for porous media the inertia impact is negligible [33,36,37]. A viscous-dominated stage of the imbibition into porous media is described by the Lucas–Washburn equation [33,34]

$$\frac{2\sigma\cos\theta}{R_s} = \frac{\phi\mu_L\dot{h}h}{K}, \tag{2}$$

where h is the wicking height, σ and μ_L are the surface tension and the dynamic viscosity of liquid, respectively, θ is the contact angle and R_s is the static pore radius of a porous structure. The wicking height h can be recalculated into the mass of imbibed liquid using

$$m(t) = \rho_L\phi A h(t), \tag{3}$$

where A is the cross-section area of a sample. Rearranging Eqs. (2) and (3), one obtains

$$\frac{m^2}{t} = \frac{4\sigma\cos\theta\rho_L^2A^2\phi}{\mu_L}\frac{K}{R_s}. \tag{4}$$

The static pore radius R_s in Eqs. (2) and (4) indicates the characteristic pore size of porous media determined using the wicking height h_{eq} at the equilibrium between the capillary and hydrostatic pressures [25,30,38]

$$\frac{2\sigma\cos\theta}{R_s} = \rho_L g h_{eq}, \tag{5}$$

where g is the gravity constant. The equilibrium height for the imbibition with the FC-72 liquid was estimated to be approximately 0.174 m and 0.923 m for the samples prepared at the freezing temperature of −80 °C and −150 °C, respectively. Due to the sample size limitation it was not possible to achieve such wicking heights experimentally. For further calculations we used the volume-weighted characteristic pore size R_{av} obtained via the mercury intrusion porosimetry.

Fig. 5 shows wicking results for the sample 80-1, 80-2, 150-1 and 150-2 in terms of the squared mass of the imbibed FC-72 liquid plotted versus time. The mass of the imbibed liquid was computed using the sample weight measurements during the imbibition and the dry sample weight measurements, and corrected in accordance with the argumentation provided in Section 2.3. The samples demonstrated various imbibition rates, see Fig. 5. Moreover, the imbibition rates differed for $-z$ and $+z$ orientations of each sample that reflected the samples anisotropy in the axial direction.

According to Fries and Dreyer [30,31], the influence of the hydrostatic pressure on wicking is negligible up to 10% of the equilibrium wicking height. In this domain when accepting an error of 3.7%, one might apply the Lucas–Washburn equation. This fraction of the equilibrium wicking height for the samples prepared at the freezing temperature of −80 °C was estimated to be 0.0174 m and recalculated into the equilibrium wicking mass m_{eq} using Eq. (3). The black horizontal solid line with the inscription 0.01 m_{eq}^2 is assigned to the squared value of 10% of the equilibrium wicking mass on Fig. 5. Below this line the linear regression of the experimental data for the samples 80-1 and 80-2 had a constant slope and was fitted via Eq. (4). For the samples prepared at the freezing temperature of −150 °C the value related to 10% of the equilibrium wicking height was estimated to be 0.0923 m. This exceeds the sample length on approximately 120%, see Table 1. Hence, for these samples Eq. (4) was fitted to the whole range of the experimental data, see Fig. 5.

Using fitting via Eq. (4), the macroscopic parameters and geometrical characteristics from Table 1, and the thermophysical properties of FC-72 liquid from Table 2, the permeabilities K_{-z} and K_{+z} for $-z$ and $+z$ sample orientations, respectively, were computed. The results are summarized in Table 1. The samples demonstrated lower permeability in $+z$ direction, i.e. when they were oriented to the liquid surface with the cone structure of the upward oriented lamellar pores. This implies that the upward orientation of the lamellae contributed to forming porous structures of lower ability to conduct the liquid than the radial orientation. The decrease of the permeability here might be also stipulated by the influence of two temperature gradients at once at the bottom of the monolith during the fabrication process, resulting in smaller pore size. As shown in Table 1, the deviations between K_{-z} and K_{+z} were found to be from 10% to 49%. These values quantify the impact of the porous structure anisotropy on the capillary transport characteristics of the samples. Higher permeability was revealed for

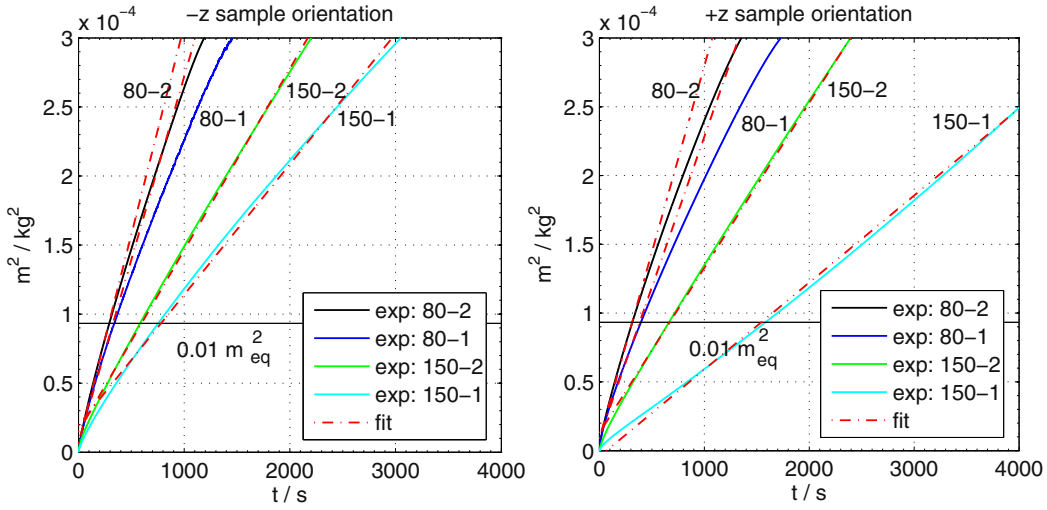

Fig. 5. The squared mass of the imbibed FC-72 liquid into the samples 80-1, 80-2, 150-1 and 150-2 versus time. The imbibition rates differs for the samples and for $+z$ and $-z$ orientations of each sample. Eq. (4) was fitted to experimental data up 10% of the equilibrium wicking height for each sample. The equilibrium wicking height corresponds to the equilibrium wicking mass. The horizontal solid line with the inscription 0.01 m_{eq}^2 is referred to the squared value of 10% of the equilibrium wicking mass for the samples 80-1 and 80-2. For the samples 150-1 and 150-2 the equilibrium wicking height exceeded the sample length, therefore, Eq. (4) was fitted to the whole range of the experimental data.

the samples prepared at the freezing temperature of −80 °C. The bigger pore size of these samples could stipulate such a result, see Section 3.1.

3.3. Imbibition at different sample orientation

The measurements of the dry sample weight and the sample weight during the imbibition were used to calculate the mass of the imbibed liquid. Fig. 6 displays the increase of the imbibed mass of the FC-72 liquid in time for the samples 80-1, 80-2, 150-1 and 150-2 at $-z$ and $+z$ orientations.

Fig. 6 shows that the smaller is the ratio d/D of the diameter of the upward oriented pores section to the overall diameter of a cylindrical sample, the smaller are the differences in wicking at $-z$ and $+z$ sample orientations. That is in accordance with our expectations. The samples with smaller d/D are less anisotropic in the axial direction and have smaller differences in permeabilities for $-z$ and $+z$ orientations, i.e. minimum K_{+z}/K_{-z}, see Table 1. Hence, for these samples we observed a minimum discrepancy of wicking results for $-z$ and $+z$ sample orientations.

A comparison of wicking results for the samples prepared at two freezing temperatures reveals significant differences in imbibition rates. The samples prepared at the freezing temperature of −80 °C demonstrated faster wicking compared to the samples prepared at the freezing temperature of −150 °C, see Fig. 6. For these samples, a time approximately twice as large was required for complete saturation with FC-72 liquid. Meanwhile, the open porosity of the samples varied only slightly, see Table 1. That is in conformity with the results of the permeability determination, see Section 3.2. The samples 80-1 and 80-2 demonstrated higher permeability compared to 150-1 and 150-2 for both sample orientations, see Table 1.

In addition, we observed larger differences in wicking at $-z$ and $+z$ orientations for the samples prepared at the freezing temperature of −150 °C than for the samples prepared at −80 °C. That was most pronounced for the samples 80-1 and 150-1 that were of the same value of d/D, see Fig. 6. This could not be compared directly for the samples 80-2 and 150-2 due to the inequality of the d/D parameter. Nevertheless, the sample 150-2 that was of a smaller d/D demonstrated a slightly larger ratio K_{+z}/K_{-z} of the permeabilities at $-z$ and $+z$ orientations compared to the sample 80-2, see Table 1.

Table 3
List of the parameters of Eq. (7).

Parameter	Equation	Physical meaning
b	$\frac{\phi R_s}{K}\frac{\mu_L}{2\sigma\cos\theta}$	$\frac{\text{viscous force}}{\text{capillary pressure}}$
c	$R_s\frac{\rho_L g}{2\sigma\cos\theta}$	$\frac{\text{gravity}}{\text{capillary pressure}}$

3.4. Theoretical prediction of wicking

In this section we provide some theoretical prediction of wicking results. We continue using the analogy of the flow through porous media to the flow through a bundle of capillary tubes, and the macroscopic approach to the description of imbibition as in Section 3.2. However, here we focus on the viscous-gravitational stage of the process.

In this domain the momentum balance for the imbibition of liquid into porous media reads as the interaction of the capillary pressure, viscous forces and hydrostatic pressure [33,36,37]

$$\frac{2\sigma\cos\theta}{R_s} = \frac{\phi\mu_L\dot{h}h}{K} + \rho_L g h. \tag{6}$$

Eq. (6) is known as the Lucas–Washburn equation with gravity effects. In order to compare the impact of the viscous force and the hydrostatic pressure on the imbibition for each sample, we introduced the parameters listed in Table 3. Some analogous parameterization has been also applied in [25,30–32]. Substituting the parameters from Table 3 into Eq. (6), one obtains

$$1 = b\dot{h}h + ch. \tag{7}$$

The theoretical model prediction was computed for wicking into each sample at $-z$ and $+z$ orientations using Eq. (7) with the parameters from Table 3, the thermophysical properties of FC-72 liquid from Table 2 and the geometrical characteristics and macroscopic parameters of the samples from Table 1. The calculated parameters of Eq. (7) are summarized in Table 4.

According to the definition of the parameter c given in Table 3, it indicates a relative influence of gravity on the imbibition that is stipulated by capillary pressure. Table 4 demonstrates that c is larger for the samples prepared at the freezing temperature of −80 °C than for the samples prepared at −150 °C. Such a result is

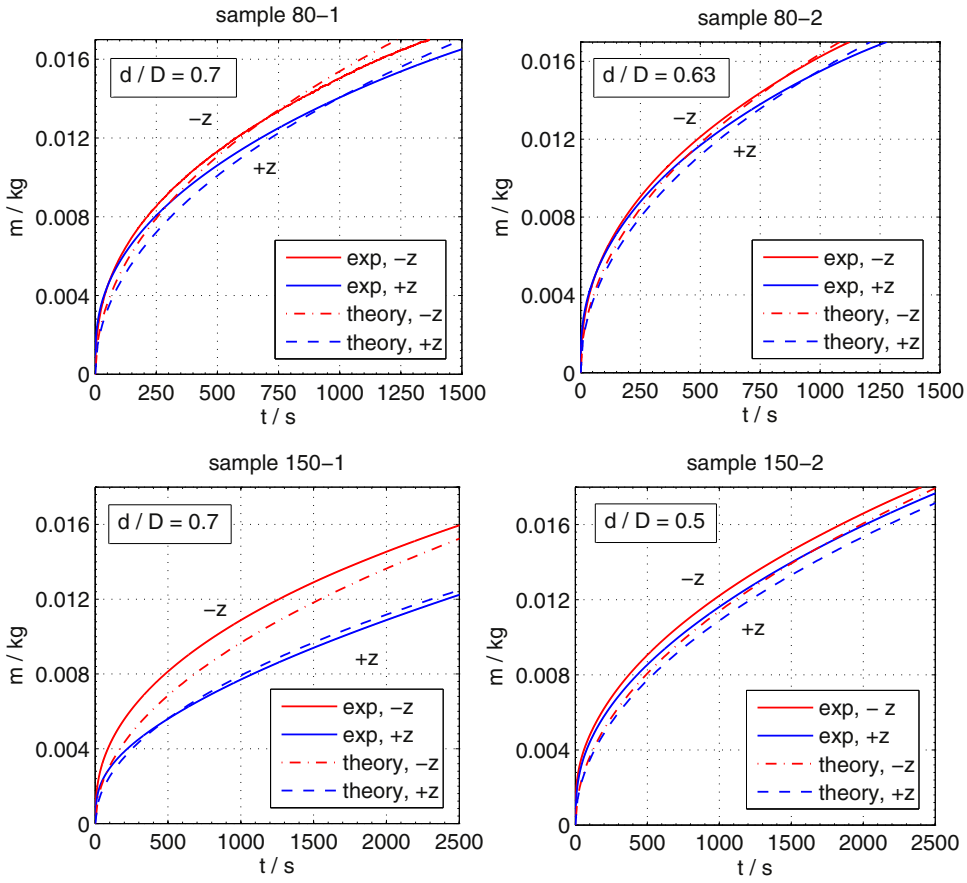

Fig. 6. The mass of the imbibed FC-72 liquid into the samples 80-1, 80-2, 150-1 and 150-2 versus time. The theoretical prediction was computed using Eq. (7) and the parameters from Table 4. The samples 80-1 and 80-2 demonstrate faster wicking compared to the samples 150-1 and 150-2. Meanwhile, the latter show the larger differences in the wicking rates at $-z$ and $+z$ sample orientations. The differences, however, become insignificant with the decrease of d/D.

Table 4
List of the parameters of Eq. (7).

Sample	b (s m^{-2}) 10^6	c (m^{-1})
−z orientation		
80-1	2.34	5.76
80-2	2.09	5.76
150-1	8.04	1.07
150-2	5.78	1.07
+z orientation		
80-1	2.86	5.76
80-2	2.34	5.76
150-1	12.0	1.07
150-2	6.33	1.07

due to a smaller pore size of the latter that ensures a higher capillary pressure. A different sample orientation does not influence the hydrostatic or capillary pressure, therefore, the parameter c varies only for different porous structures. Meanwhile, for each sample the parameter b is larger at $+z$ orientation than at $-z$, see Table 4. This parameter indicates the relative influence of the viscous force on the imbibition. Such a result implies that the viscous force has a stronger influence on the imbibition at $+z$ sample orientation. This is in conformity with the permeability results that showed higher values for the samples at $-z$ orientation. The parameter b contains a combination of the macroscopic parameters unique for each porous structure. Due to that b also varies for each sample.

The results of the theoretical model prediction were plotted in Fig. 6. The theoretical prediction is in good agreement with the experimental data. That indicated that the macroscopic model that has been primarily developed for the description of the imbibition in a homogeneous porous structure could also serve as a simple tool to predict it for some anisotropic structures. Nevertheless, in this case the preliminary characterization of the anisotropy and directional determination of the macroscopic parameters are necessary.

4. Conclusion

Anisotropic porous silicon oxycarbide (SiOC) cylindrical monoliths were fabricated using a freeze-casting method. The lamellar pore structures with an axial anisotropy were prepared at two different freezing temperatures (−80 °C and −150 °C) and revealed similar porosity but different pore size distribution. To characterize the capillary transport abilities of the porous samples, vertical wicking experiments were performed. Using sample weight measurement during imbibition, we evaluated the increase of the mass of the imbibed liquid with time. The permeability was determined using results at the viscous-dominated stage of wicking. The deviations of permeability at two different sample orientations were found to vary from 10% to 49%. They are larger for the samples prepared at the freezing temperature of −150 °C that revealed smaller average pore size. These values quantified the impact of the axial anisotropy on the capillary transport abilities of the porous structures. Correspondingly, the larger differences in wicking at two sample orientations were also observed for these samples. However, the complete saturation with the experimental liquid occurred approximately twice as fast as for the samples prepared at the freezing temperature of −80 °C. Such a result is due to the higher permeability of the samples that could be stipulated by

bigger pores. In addition, the experiment data was compared with a theoretical prediction performed using the Lucas–Washburn equation with gravity effects. The wicking results for each sample at both sample orientation demonstrated a good agreement with the theoretical prediction. This implies applicability of macroscopic modelling as a simple tool to predict wicking in some anisotropic porous structures. It requires, however, preliminary characterization and directional determination of macroscopic parameters of a porous medium.

Acknowledgement

This work was supported by the German Research Foundation (DFG) within the Research Training Group GRK 1860 "Micro-, meso- and macroporous nonmetallic Materials: Fundamentals and Applications" (MIMENIMA).

References

[1] L.L. Vasiliev, Heat pipes in modern heat exchangers, Appl. Therm. Eng. 25 (2005) 1–19.
[2] A. Sommers, Q. Wang, X. Han, C. T'Joen, Y. Park, A. Jacobi, Ceramics and ceramic matrix composites for heat exchangers in advanced thermal systems – a review, Appl. Therm. Eng. 30 (2010) 1277–1291.
[3] A. Julbe, D. Farrusseng, C. Guizard, Porous ceramic membranes for catalytic reactors – overview and new ideas, J. Membr. Sci. 181 (2001) 3–20.
[4] M. Nacken, G.V. Baron, S. Heidenreich, S. Rapagna, A. D'Orazio, K. Gallucci, J.F.M. Denayer, P.U. Foscolo, New DeTar catalytic filter with integrated catalytic ceramic foam: catalytic activity under model and real bio syngas conditions, Fuel Process. Technol. 134 (2015) 98–106.
[5] N. Gao, A. Li, C. Quan, F. Gao, Hydrogen-rich gas production from biomass steam gasification in an updraft fixed-bed gasifier combined with a porous ceramic reformer, Int. J. Hydrogen Energy 33 (2008) 5430–5438.
[6] J. Adler, Ceramic diesel particulate filters, Int. J. Ceram. Technol. 2 (6) (2005) 429–439.
[7] S. Sarkar, S. Bandyopadhyay, A. Larbot, S. Cerneaux, New clay-alumina porous capillary supports for filtration application, Int. Membr. Sci. 392-393 (2012) 130–136.
[8] E.C. Hammel, O.L.R. Ighodaro, O.I. Okoli, Processing and properties of advanced porous ceramics: an application based review, Ceram. Int. 40 (2014) 15351–15370.
[9] D.E. Jaekle, Propellant management device conceptual design and analysis: galleries, in: AIAA-97-2811, 1997.
[10] M. Wollen, F. Merino, J. Schuster, C. Newton, Cryogenic propellant management device: conceptual design study, in: NASA/CR-010-216777, 2010.
[11] D.J. Chato, M.T. Kudlac, Screen channel liquid acquisition devices for cryogenic propellants, in: AIAA-2002-3983, 2002.
[12] P. Behruzi, J. Klatte, G. Netter, Passive phase separation in cryogenic upper stage tanks, in: Proceeding of 49th AIAA/ASME/SAE/ASEE Joint Propulsion Conference, San Jose, USA, 2013.
[13] M. Conrath, Y. Smiyukha, E. Fuhrmann, M. Dreyer, Double porous screen element for gas–liquid phase separation, Int. J. Multiph. Flow 50 (2013) 1–15.
[14] M. Ulbricht, O. Schuster, W. Ansorge, M. Ruetering, P. Steiger, Influence of the strongly anisotropic cross-section morphology of a novel polyethersulfone microfiltration membrane on filtration performance, Sep. Purif. Technol. 57 (2007) 63–73.
[15] T. Liu, M. Huang, X. Li, C. Wang, C.X. Gui, Z.Z. Yu, Highly compressible anisotropic graphene aerogels fabricated by directional freezing for efficient absorption of organic liquids, Carbon 100 (2016) 456–464.
[16] S.Y. Chung, M.A. Elrahman, D. Stephan, Investigation of the effects of anisotropic pores on material properties of insulating concrete using computed tomography and probabilistic methods, Energy Build. 125 (2016) 122–129.
[17] P. Colombo, Engineering porosity in polymer-derived ceramics, J. Eur. Ceram. Soc. 28 (7) (2008) 1389–1395.
[18] A. Studart, U.T. Gonzenbach, E. Tervoort, L.J. Gauckler, Processing routes to macroporous ceramics: a review, J. Am. Ceram. Soc. 89 (6) (2016) 1771–1789.
[19] E.O. Einset, Capillary infiltration rates into porous media with application to Silcomp processing, J. Am. Ceram. Soc. 79 (2) (1996) 333–338.
[20] S. Kumar, A. Kumar, A. Shukla, A.K. Gupta, R. Devi, Capillary infiltration studies of liquids into 3D-stitched C–C preforms. Part A: Internal pore characterization by solvent infiltration, mercury porosimetry, and permeability studies, J. Eur. Ceram. Soc. 2 (9) (2009) 2643–2650.
[21] S. Kumar, A. Kumar, R. Devi, A. Shukla, A.K. Gupta, Capillary infiltration studies of liquids into 3D-stitched C–C preforms. Part B: Kinetics of silicon infiltration, J. Eur. Ceram. Soc. 29 (2009) 2651–2657.
[22] K. Okada, S. Uchiyama, T. Isobe, Y. Kameshima, A. Nakajima, T. Kurata, Capillary rise properties of porous mullite ceramics prepared by an extrusion method using organic fibers as the pore former, J. Eur. Ceram. Soc. 29 (2009) 2491–2497.
[23] K. Okada, A. Imase, T. Isobe, A. Nakajima, Capillary rise properties of porous geopolymers prepared by an extrusion method using polylactic acid (PLA) fibers as the pore formers, J. Eur. Ceram. Soc. 31 (2011) 461–467.
[24] H. Zhang, P. D'Angelo Nunes, M. Wilhelm, K. Rezwan, Hierarchically ordered micro/meso/macroporous polymer-derived ceramic monoliths fabricated by freeze-casting, J. Eur. Ceram. Soc. 36 (2016) 51–58.
[25] Y. Grebenyuk, M.E. Dreyer, Wicking of liquid nitrogen into superheated porous structures, Cryogenics 78 (2016) 27–39.
[26] A. Al-Shareef, P. Neogi, B. Bai, Force based dynamic contact angles and wetting kinetics on a Wilhelmy plate, Chem. Eng. Sci. 99 (2013) 113–117.
[27] E. Rame, The interpretation of dynamic contact angles measured by the Wilhelmy plate method, J. Colloid Interface Sci. 185 (1997) 245–251.
[28] S. Whitaker, Flow in porous media I: a theoretical derivation of Darcy's law, Transp. Porous Media 1 (1986) 3–25.
[29] W.G. Gray, K. O'Neill, On general equations for flow in porous media and their reduction to Darcy's law, Water Resour. Res. 12 (2) (1976) 148–154.
[30] N. Fries, K. Odic, M. Conrath, M. Dreyer, The effect of evaporation on the wicking of liquids into a metallic weave, J. Colloid Interface Sci. 321 (2008) 118–129.
[31] N. Fries, M. Dreyer, An analytic solution of capillary rise restrained by gravity, J. Colloid Interface Sci. 320 (2008) 259–263.
[32] N. Fries, M. Dreyer, Dimensionless scaling methods for capillary rise, J. Colloid Interface Sci. 338 (2009) 514–518.
[33] E.W. Washburn, The dynamics of capillary flow, Phys. Rev. 17 (3) (1921) 273–283.
[34] R. Lucas, Ueber das Zeitgesetz des kapillaren Aufstiegs von Fluessigkeiten, Kolloid Z. 23 (1918) 15–22.
[35] M. Stange, M. Dreyer, H. Rath, Capillary driven flow in circular cylindrical tubes, Phys. Fluids 15 (2003) 2587–2601.
[36] M. Lago, M. Araujo, Capillary rise in porous media, Physica A 289 (2001) 1–17.
[37] R. Masoodi, K.M. Pillai, P.P. Varanasi, Darcy's law based models for liquid absorption in polymer wicks, AIChE J. 53 (11) (2007) 2769–2782.
[38] R. Masoodi, K.M. Pillai, P.P. Varanasi, Role of hydraulic and capillary radii in improving the effectiveness of capillary model in wicking, in: Proceedings of FEDSM2008. 2008 ASME Fluids Engineering Conference, Jacksonville, Florida, USA, 2008.